Journal of Alloys and Compounds 753 (2018) 138–148

Contents lists available at ScienceDirect

Journal of Alloys and Compounds

journal homepage: http://www.elsevier.com/locate/jalcom

Modulation of the Pr^{3+} luminescence in the $SrTi_{1-x}Zr_xO_3$ solid solution

Germán López-Pacheco [a], María Elena Villafuerte-Castrejón [a], Enrique Barrera-Calva [b], Federico González [b, *]

[a] Instituto de Investigaciones en Materiales, Universidad Nacional Autónoma de México, A.P. 70-360, Ciudad de México, Mexico
[b] Departamento de Ingeniería de Procesos e Hidráulica, Universidad Autónoma Metropolitana-Iztapalapa, A.P. 55-534, Ciudad de México, Mexico

ARTICLE INFO

Article history:
Received 26 December 2017
Received in revised form
11 April 2018
Accepted 12 April 2018
Available online 13 April 2018

Keywords:
Ceramics
Optical properties
Pr^{3+}-luminescence
Ligand-to-metal charge transfer
X-ray diffraction

ABSTRACT

In this work ceramic samples of $Sr_{0.9955}Pr_{0.003}Ti_{1-x}Zr_xO_3$ ($0.0 \leq x \leq 1.0$) solid solution were synthesized by the Pechini method. Samples calcined at 800 °C for 1 h were characterized by X-ray diffraction; scanning electron microscopy, diffuse reflectance and photoluminescent spectroscopies. The compounds exhibit three different crystal perovskite-like structures as a function of the chemical composition: Cubic ($0.0 \leq x \leq 0.2$), tetragonal ($0.3 \leq x \leq 0.6$) and orthorhombic ($0.7 \leq x \leq 1.0$). The substitution of Ti^{4+} by Zr^{4+} in the solid solution results in an increase in the energy of the transition associated with the host. The presence of a ligand-to-metal charge transfer state between O^{2-} and Ti^{4+} and its effect on the Pr^{3+} luminescence is shown. The photoluminescence response of Pr^{3+} is explained by using the chemical shift model. A remarkable consequence of the chemical variation in the series compounds, is the color-modulation of the emission under excitation at 447 nm ($^3H_4 \rightarrow {}^3P_2$). It goes from a dominant red emission ascribed to the $^1D_2 \rightarrow {}^3H_4$ transition to a dominant greenish-blue emission ascribed to the $^3P_0 \rightarrow {}^3H_4$. Finally, the color coordinates associated with the emission for the entire series are plotted in the CIE 1931 color space.

1. Introduction

For many years, ceramics with perovskite-like structure and ABO_3 general formula have been subject of extensive scientific interest due to their variety of physical properties: magnetics, electrics or even optics [1–6]. For these properties, the fundamental variable governing their performance is the crystalline structure. The prototypically perovskite structure has the cubic symmetry *Pm-3m*. The B cation is at the cube corner and is six-fold coordinated by oxygen ions forming a BO_6 octahedron; whereas the A cation is at the cube center surrounded by eight BO_6 octahedra and coordinated by twelve O^{2-} anions [5,6].

Luminescent properties are one of the most interesting and important properties investigated in material science. In this scientific field, the lanthanide luminescent-activated materials usually designated as phosphors, are subject of much interest due to the wide range of applications in displays, lasers, fluorescent lamps and solid-state lighting among others [7–9]. Each specific application should demand a clear understanding of the ion activator-host interaction. In trivalent lanthanides, it is generally assumed that they preserve their ion-free energy levels diagram no matter where they are incorporated, and consequently only a superposition of their levels and those of the host, need to be considered. We are convinced this picture is in many cases oversimplified as it has been demonstrated previously [10–14]. Particularly, Pr^{3+} doping oxide based-ceramics show a notable change on the luminescence properties of lanthanide ion due to the chemical composition of the ceramic host. For example, the luminescent response of Pr^{3+} incorporated into $CaTiO_3$ and $CaZrO_3$ shows unique features [15]. Pr^{3+}-doped $CaTiO_3$ exhibits a strong red emission associated with the $^1D_2 \rightarrow {}^3H_4$ transition. On the other hand, Pr^{3+}-doped $CaZrO_3$ shows a greenish-blue emission ascribed to the $^3P_0 \rightarrow {}^3H_4$ transition.

Following the virtual recharge mechanism proposed by Reut and Ryskin [16], involving a charge exchange from a trivalent lanthanide (with “relatively low” fourth ionization potential) to metal in oxidizing-character host lattices, some authors proposed an explanation to describe the $^3P_0 \rightarrow {}^1D_2$ de-excitation process in titanates [17,18]. The central component of this model is a metal-to-metal charge transfer (MMCT) state (also known as intervalence charge transfer (IVCT) state). According to the MMCT model, in Pr^{3+} doped titanates, there is an MMCT state Pr^{4+}-O^{2-}-Ti^{3+} near to the

* Corresponding author.
E-mail address: fgg@xanum.uam.mx (F. González).

https://doi.org/10.1016/j.jallcom.2018.04.156
0925-8388/

Pr^{3+}-O^{2-}-Ti^{4+} configuration excited states. Thus, after the promotion of an *f* electron of Pr^{3+} through the MMCT, the relaxation occurs from this "state" and then the electron returns to the $^1D_2$ excited level of Pr^{3+}. This process could produce a "quenching" of $^3P_0$ level emission, depending on the charge transfer level position respect to the $^1D_2$ and $^3P_0$ levels. However, Barandarián and coworkers [19] using state-of-the-art ab initio calculations have recently shown that the intermediate state responsible for the nonradiative decay from $^3P_0$ to $^1D_2$ in Pr^{3+}-doped $CaTiO_3$ is an O^{2-}-to-Ti^{4+} ligand-to-metal charge transfer (LMCT) state. Moreover, according to their results, the O^{2-}-to-Ti^{4+} LMCT state could rule out the necessity of the Pr^{3+}-Ti^{4+} MMCT state to explain the dominant red luminescence assigned to transitions from the $^1D_2$ level to the $^3H_4$ ground state of the Pr^{3+}. Supporting this fact, some of us have recently reported experimental results showing the favoring of the $^1D_2 \rightarrow {}^3H_4$ transition when $SrZrO_3$:Pr^{3+} samples containing low concentrations of Ti^{4+} are excited through the O^{2-}-to-Ti^{4+} LMCT state [20].

Regardless of whether the red emission in the titanates is due to the one or the other charge transfer state; or if it is due to an intricate process in which both charge transfer states operate simultaneously, it is important for the reader to keep in mind the peculiar luminescent behavior of the Pr^{3+}, and how its luminescent properties are strongly dependent on the crystalline and electronic host structures, which in turn, and in our opinion, are ruled by the chemical composition. Despite that important effect of the chemical composition on the luminescent features of Pr^{3+}, noticeably only few papers have been reported on titanate Pr^{3+}-doped solid-solutions, namely (Ca,Sr)TiO_3 [21], (Ca,Sr,Ba)TiO_3 [22] and Ca(Ti,Zr)O_3 [23] in which the authors tried to get a comprehensive explanation about the above-mentioned factors and their effect on the luminescent properties of the Pr^{3+}. Also, although there are studies about $SrTiO_3$ (STO) and $SrZrO_3$ (SZO) doped with Pr^{3+} [20,21,24] and other lanthanide ions [25,26], until now there are no any work about $SrTi_{1-x}Zr_xO_3$ solid-solution (STZO) doped with Pr^{3+}. Thus, it would be of scientific interest to know how the luminescent response of Pr^{3+} changes through a solid-solution system having different crystal structures and chemical compositions, in order to get insight into the relationship between the Pr^{3+}-luminescent properties and the crystalline and electronic host structures.

STZO belongs to the perovskite family compounds. On one hand, it exists the STO which has the phase transition from tetragonal (*I*4/*mcm*) to cubic (*Pm-3m*) at 105 K [27]. On the other, SZO have three phase transitions; orthorhombic (*Pnma*) to "pseudo-tetragonal" (*Imma*) at 1023 K, "pseudo-tetragonal" (*Imma*) to tetragonal (*I*4/*mcm*) at 1113 K, and finally tetragonal (*I*4/*mcm*) to cubic (*Pm-3m*) at 1343 K [28]. Regarding the phase diagram of the STZO, there are some experimental reports about it. In one of them, the authors used synchrotron X-ray and neutron powder diffraction techniques [29]. The others are based on studies of systems having phase transitions of analogues structures; *Pm-3m*, *I*4/*mcm*, *R*3*c*, *Imma* and *Pnma* as those exhibited by the end compositions of STZO; and on the analysis of their mechanical properties [30,31]. However, despite all this effort, no consensus exists yet, about the actual phase-transition in the STZO system. Some authors stated that there are three phase-transition, involving four different symmetries; *Pnma*, *Imma*, *I*4/*mcm* and *Pm-3m* [30], but in opposition to this result, other authors have described the system as having only two phase-transition, and therefore involving three symmetries; *Pnma*, *I*4/*mcm* and *Pm-3m* [29]. In any case, the structure varieties and phase transitions involved in this system may result in an interesting lanthanide doped solid-solution which deserves to be investigated, since luminescence and structure are strongly correlated.

Of interest for any research that intends to investigate the interaction between a host and a dopant, is the location of the energy levels of the dopant relative to the electronic structure of the host. Nowadays, there is a reasonable phenomenological model explaining this issue for the lanthanide ions, being accomplished by Thiel [32–34] and Dorenbos [35–37]: the chemical shift model (CSM).

In the present work, we take advantage of the approach of the CSM formulated by Dorenbos to estimate the binding energies of the electrons in 4f-states and in the host band states relative to the same reference: the vacuum energy. This approach of the CSM makes easy the comparison of many materials, some of them similar, and allows to rationalize the effect of the host on the optical properties of the lanthanide ions [10,13,14,35–38].

On the other hand, in recent years, the development of multicolor emitting phosphors for solid-state lighting applications, has attracted great attention [9,39–41]. Usually, phosphors are the combination of a host lattice doped with low concentrations of activator ions. The activator ions have their own intrinsic luminescent characteristics which could be added to those ones of the host to produce the desirable emission effect. The most common activator ions used for solid-state lighting devices, are Ce^{3+}, Tb^{3+} and Eu^{2+} [39,42]. However, the host lattice characteristics ultimately determine the optical properties of a phosphor. Many efforts have been made in the search of appropriated phosphors which would be able to transform ultraviolet or blue light into a combination of red, green and blue light to produce white light [9,39]. For this reason, it is necessary to assess the possibility that Pr^{3+}-doped STZO solid-solution could be a suitable oxide phosphor with optimal luminescent properties for solid-state lighting.

In this work we investigate the crystalline structure and the luminescent features of the solid-solution $Sr_{0.9955}Pr_{0.003}Ti_{1-x}Zr_xO_3$ as function of the Ti/Zr relative concentration. In order to achieve our aim, powder compounds of the SPTZO solid-solution were synthesized by the Pechini method. They were characterized by X-ray Diffraction (XRD); Scanning Electron Microscopy (SEM), Energy Dispersive X-Ray Spectroscopy (EDS), reflectance and luminescent spectroscopies. Finally, the observed modulation of Pr^{3+} greenish-blue and red emission ascribed to the $^3P_0 \rightarrow {}^3H_4$ and $^1D_2 \rightarrow {}^3H_4$ transitions, respectively, as well as the effect of the host lattice on the phosphor luminescent properties were analyzed by using the approach of the CSM to account for the Pr^{3+} luminescence properties along the entire $Sr_{0.9955}Pr_{0.003}Ti_{1-x}Zr_xO_3$ solid-solution.

2. Experimental

2.1. Ceramic powders synthesis

Polycrystalline ceramic powders of the $Sr_{0.9955}Pr_{0.003}Ti_{1-x}Zr_xO_3$ ($0.0 \leq x \leq 1.0$) solid-solution (SPTZO) were synthetized by the Pechini method [43]. A small concentration at 0.3% mol of Pr^{3+} was incorporated into the STZO solid solution series in a way to preserve the charge balance. The starting raw materials used were $Sr(NO_3)_2$ (99%, Sigma-Aldrich), $Pr(NO_3)_3 \cdot 6H_2O$ (99.9%, Sigma-Aldrich), $Ti(OCH(CH_3)_2)_4$ (97%, Sigma-Aldrich), $Zr(O(CH_2)_2\text{-}CH_3)_4$ (70% in 1-propanol, Sigma-Aldrich), citric acid $C_3H_4(COOH)_3$ (ACS reagent, Sigma-Aldrich), ethylene glycol $C_2H_6O_2$ (ACS reagent, Sigma-Aldrich) and absolute ethanol (ACS reagent, JT Baker). In a typical Pechini synthesis, the titanium isopropoxide and zirconium

propoxide were dissolved in absolute ethanol under continuous stirring, immediately after that, citric acid (molar ration 1:4, amount of metals: citric acid) and ethylene glycol was added for stabilization of the Zr^{4+} and Ti^{4+} cations. This solution was stirred by 1 h at 60 °C. Apart, strontium nitrate and praseodymium nitrate were dissolved in deionized water under stirring by 30 min at room temperature. This last aqueous solution was blended with the former alcoholic solution. Then, the temperature of the final solution was raised to 70 °C for induce the evaporation of the solvents giving place to a viscous yellowish solution. For promoting polymerization of the blend, the temperature was set at 90 °C until a resin was obtained. This resin was then pre-calcinated in an oven at 300 °C for 1 h obtaining a dark-brown powder. Finally, the pre-calcined powders were further calcined at 800 °C for 1 h in air.

2.2. Characterization

The crystal structure characterization of SPTZO powders were carried out from X-ray patterns measured in a Bruker D-8 Advance diffractometer fitted with a CuK_α X-ray tube and a one-dimensional position-sensitive silicon strip detector (Bruker, Lynxeye) [44]. The diffraction patterns were measured between 20° and 110°, with a 2θ step of 0.020415°, for 76.8 s per point. Crystalline structures were refined by the Rietveld method using a fundamental parameters approach [45]. During the refinements, as implemented in the TOPAS code, version 4.2 [46]. SRM-NIST 660 b (LaB_6) [47] was used to model the contributions of the instrument. The Cu-K_α X-ray emission profile was modeled with the one reported by G. Hölzer et al. [48]. The parameters used in refinements included polynomial terms for modeling of the background, the lattice parameters, terms indicating the position and intensity of the "tube tails", specimen displacement, structural parameters, and the width of a Lorentzian profile for modeling the average crystallite size. Last feature was modeled in reciprocal space with a symmetrized harmonics expansion [49]. The standard deviations, given in parentheses in the text, show the variation in the last digit; when they correspond to Rietveld refined parameters [50]. The morphology and EDS spectra of SPTZO powders were performed by SEM in a Field Emission Scanning Electron Microscope (JEOL JSM-7600F). The diffuse reflectance spectra measurements were recorded using a Praying Mantis cell-type (Harrick Scientific Products Inc.) in the range of 200 nm to 700 nm and performed in a Cary 5 spectrophotometer. Once that spectra were measured, a mathematical analysis was performed to calculate the energy of the bandgap. An Edinburgh Instruments FSP920 spectrofluorometer based on the method of single photon counting, equipped with a 450 W xenon lamp as a CW light source and an R928P PMT as a detector, was used to record emission and excitation spectra. All the excitation and emission spectra were corrected for the wavelength dependent responses of the Xe lamp and the detector, respectively.

3. Results and discussion

3.1. Crystal structure

The XRD patterns of the SPTZO powders synthetized by the Pechini method and calcined at 800 °C for 1 h are shown in Fig. 1. All samples show a pure perovskite-like structure. However, symmetry changes appear when chemical composition of the solid solution varies. In Fig. 1(a), the diffractograms are grouped according to their crystal structure. It is cubic from x = 0.0 to 0.2 matching with PDF card 04-007-0044 of $SrTiO_3$; tetragonal from x = 0.3 to 0.6 matching with PDF card 01-070-5452 of $SrZr_{0.5}Ti_{0.5}O_3$ and orthorhombic from x = 0.7 to 1.0 matching with PDF card 04-014-8276 of $SrZrO_3$. Regarding the phase diagram, a previous work considers that there are two [29] phase-transitions and other considers three [30]. Due to this discrepancy, in this work it was very important to analyze and establish the crystal structure and phase transitions occurring in the SPZTO solid solution, with the final purpose to assess the probably impact on the optical properties.

In Fig. 1 (b) representative two-theta section of XRD patterns of SPTZO powders is illustrated. In b), the evolution of the (100) and (111) reflections is presented. The indexed peak for cubic structure (100) disappear in tetragonal structure and reappear in orthorhombic structure as the (002) peak. The indexed peak for the cubic structure is (111), (202) for tetragonal and finally (103) and (022) for orthorhombic. In Fig. 1 (c), the most intense reflection for all crystal symmetries is shown. The systematic shift toward lower angles of the reflection maximum as Zr^{4+} content (x) increases, is associated with the enlargement of the crystal cell, which is consistent with the fact that Zr^{4+} has a larger ionic radius than Ti^{4+}. According to Shannon in a VI-coordination the ionic radii of Zr^{4+} and Ti^{4+} are 0.72 Å and 0.605 Å, respectively [51].

To get more insight into the effect on the crystal structural features as a function of chemical composition such as the cell parameters and the average crystallite size, Rietveld analyses were performed for all samples. In the samples that exhibit cubic structure, the unit cell was modeled with the symmetry described by the space group *Pm-3m* (No. 221). In the samples having tetragonal structure, the unit cell was modeled with the symmetry described by the space group *I4/mcm* (No. 140). Finally, in the samples which crystallize in the orthorhombic structure, the unit cell was modeled with the symmetry described by the space group *Pnma* (No. 62). In Table 1 are summarized the atomic position for each ion according to the space group.

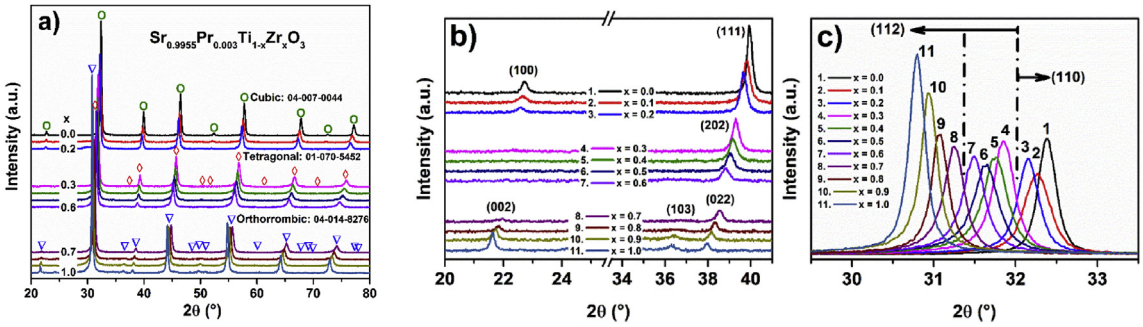

Fig. 1. XRD patterns of SPTZO powders calcinated at 800 °C for 1 h as a function of x for different 2θ intervals. (a) 20°–80°, (b) 20°–41°, and (c) 29.5°–33.5°.

Table 1
Atomic position of ions for the SPTZO powders Rietveld refinement [29,52]

Space group	Sr^{2+}/Pr^{3+}	Ti^{4+}/Zr^{4+}	O^{2-}
Pm-3m	(½, ½, ½)	(0, 0, 0)	(½, 0, 0)
I4/mcm	(0, ½, ¼)	(0, 0, 0)	(0, 0, ¼) (x, x+½, 0)[a]
Pnma[b]	(x_{Sr}, ¼, y_{Sr})[c]	(0, 0, 0)	(x_{O1}, ¼, y_{O1})[c] (x_{O2}, y_{O2}, z_{O2})[c]

[a] Initial value of x used for refinement was that one reported in Table 1 of ref. [29] for $SrTi_{0.5}Zr_{0.5}O_3$.
[b] We transform the *Pbnm* non-conventional setting of space group 62 reported in [29], into its standard setting *Pnma*.
[c] Initial values for the refinable coordinates were those reported in Table 1 of ref. [29] for $SrTi_{0.2}Zr_{0.8}O_3$.

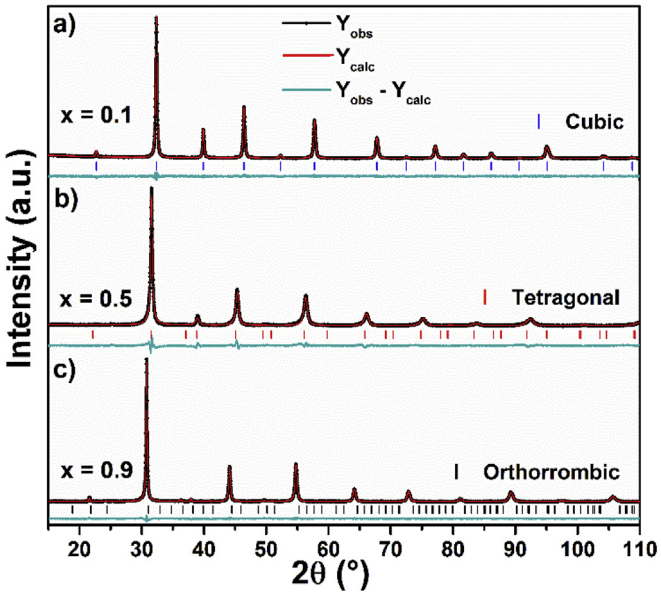

Fig. 2. Rietveld refinement plots of SPTZO powders with x = a) 0.1 - cubic, b) 0.5 – tetragonal and c) 0.9 – orthorhombic synthesized by the Pechini method and calcinated at 800 °C for 1 h.

The good agreement between experimental data and the calculated data obtained from the model, can be seen in Fig. 2. In this figure, the result of Rietveld refinements of three representative samples containing 10 mol%, 50 mol% and 90 mol% of Zr^{4+} are plotted.

Table 2 exhibits the results of the Rietveld refinement: the average crystallite size, the lattice parameters, the R_{wp} values; also,

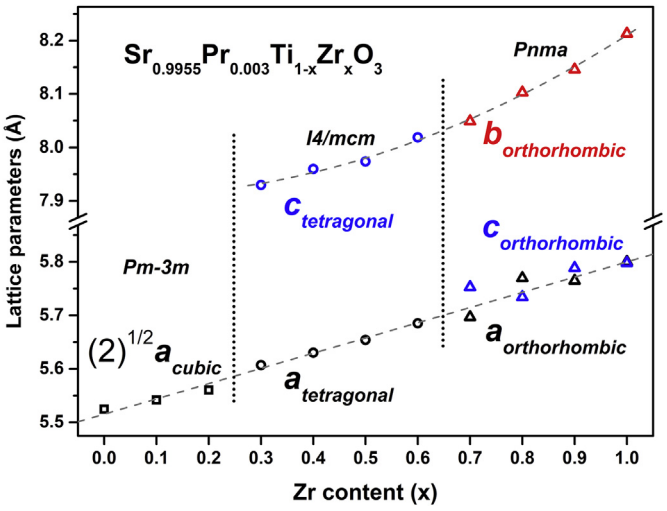

Fig. 3. Lattice parameters of SPTZO powders calcinated at 800 °C for 1 h determined by Rietveld refinements as function of x. Doted vertical lines indicate the composition regions for each crystal phase. The cubic cell parameter has been appropriately scaled by a factor of $\sqrt{2}$. Notice the break in the vertical axis. The gray dashed-lines are only indicative for the reader.

are included the distances between Ti^{4+}/Zr^{4+} and O^{2-}. The average crystallite size values for all compositions are in the nanometric scale and; moreover, the average crystallite size tends to decrease as x increases, and reach a minimum for x = 0.6, the last composition having tetragonal structure. After that, the crystallite size increases again and reach a new maximum for x = 1.0. Regarding the R_{wp} values, they are lower than 10%, indicating appropriate refinements [53]. The observed increase in the interionic distance between Ti^{4+}/Zr^{4+} and O^{2-} as the zirconium content increases, is consistent with the enlargement of the unit cell, i.e. increase of the cell parameters (see Fig. 3), since Zr^{4+} has a larger ionic radius than Ti^{4+}, as above-mentioned.

In Fig. 3 is shown the evolution of the refined lattice parameters (see Table 2) as a function of x. However, to illustrate in a unified way the evolution of those parameters as the Ti^{4+}/Zr^{4+} composition changes, in the Fig. 3 the *a*-cubic lattice parameter was scaled by a factor of $\sqrt{2}$. The a_{cubic} scaled, a_{tetra} and the a_{ortho} lattice parameter show a continuous change, despite the *Pm-3m* → *I4/mcm* transition from x = 0.2 to x = 0.3, and the *I4/mcm* → *Pnma* transition from x = 0.6 to x = 0.7. Similar behavior is observed for the c_{tetra} and b_{ortho} lattice parameters. The sequence of the crystal structures at room temperature for the SPTZO solid-solution is as follows: cubic from x = 0.0 to x = 0.2, tetragonal from x = 0.3 to x = 0.6 and orthorhombic from x = 0.7 to x = 1.0. This behavior is in agreement with

Table 2
Rietveld refinement results for the SPTZO powders calcinated at 800 °C for 1 h.

x (mol)	Space group	Crystallite size (nm)	a (Å)	b (Å)	c (Å)	*d[(Ti/Zr)-O]*[a] (Å)	R_{wp} (%)
0.0	*Pm*-3m	53.3(3)	3.90653(6)	–	–	1.95327(3)	7.52
0.1	*Pm*-3m	33.1(2)	3.91865(9)	–	–	1.95932(4)	7.13
0.2	*Pm*-3m	37.2(3)	3.930(2)	–	–	1.96588(6)	9.27
0.3	*I4/mcm*	37.1(4)	5.6070(2)	–	7.9291(8)	1.9824(6)	9.15
0.4	*I4/mcm*	29.6(3)	5.6302(3)	–	7.9620(9)	1.9946(7)	9.62
0.5	*I4/mcm*	27.8(3)	5.6600(5)	–	7.9787(7)	2.0080(9)	8.44
0.6	*I4/mcm*	22.4(2)	5.6896(6)	–	8.0226(9)	2.0259(1)	9.76
0.7	*Pnma*	25.3(3)	5.6965(8)	8.0546(8)	5.7643(9)	2.053(24)	8.71
0.8	*Pnma*	34.5(3)	5.7802(6)	8.1105(5)	5.7287(6)	2.053(12)	7.51
0.9	*Pnma*	39.6(4)	5.7584(5)	8.1537(4)	5.7958(5)	2.080(13)	7.02
1.0	*Pnma*	51.7(4)	5.8007(15)	8.2145(5)	5.7998(14)	2.090(14)	7.16

[a] When the distance between Ti/Zr and O in the $(Ti/Z)O_6$ octahedron has more than one value, average is reported.

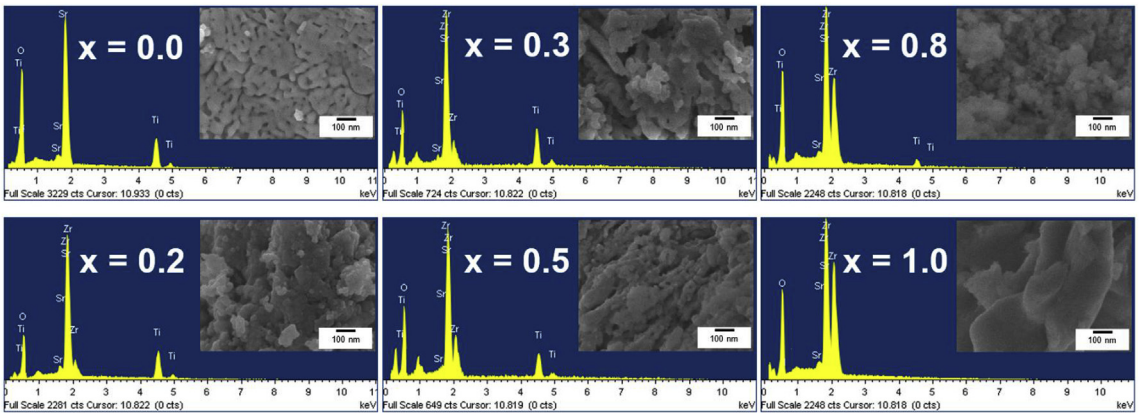

Fig. 4. SEM images and EDS microanalysis for $Sr_{0.9955}Pr_{0.003}Ti_{1-x}Zr_xO_3$, x = 0.0, 0.2, 0.3, 0.5, 0.8 and 1.0 samples.

the work where only two phase-transitions are seen [29]. There is only a small variation in the composition intervals.

In Fig. 4 are shown the SEM images and EDS spectra of SPTZO samples calcined at 800 °C for 1 h at different structure and x composition (Zr content); x = 0.0 and 0.2 (cubic), x = 0.3 and 0.5 (tetragonal), and 0.8 and 1.0 (orthorhombic). The SEM images revel the homogeneous dispersion of particles. For the sample with x = 0.0, the grains are round-shaped and form agglomerates. The average crystallite size is around 100 nm. For samples containing both, Zr^{4+} and Ti^{4+}, the powders are made of agglomerates of equiaxial round-shaped particles. Their average crystallite sizes are approximately between 50 nm and 100 nm. Finally, for the sample with x = 1.0, the particles show again an increase of the grain size. These particles are not round shaped like the other samples. The substitution of Ti^{4+} by Zr^{4+} in the solid-solution, results in a decrease in the average crystallite size. Finally, in zirconium-rich samples, an increase in average crystallite size is observed. The average crystallite sizes agree with data calculated from Rietveld refinement. The EDS spectra show the presence of strontium (Sr), titanium (Ti), zirconium (Zr) and oxygen (O). The intensity of the titanium peak decreases accordingly as the amount of Zr^{4+} increases through the solid-solution.

3.2. Optical properties

Regarding the SPTZO solid-solution samples, the substitution of Ti^{4+} for Zr^{4+} in STO is supposed to impact the optical properties of materials. The most obvious effect should be the modification of the energy band gap along the solid-solution, since it is well-known the significant difference in the energy band gap of STO and SZO [10,54]. Diffuse reflectance spectra measurements of SPTZO samples were performed to determine the changes in the absorbance as the composition of the solid-solution compounds is modified. The UV–visible (230 nm–600 nm) absorption spectra of SPTZO powders are shown in Fig. 5. It is observed a broad band for almost all ceramic powders in the UV range, from 230 nm to 400 nm. The absorption edges show a shift to lowest wavelength from x = 0.0 to x = 1.0, i.e., as Zr^{4+} content increases. This shifting toward shorter wavelengths has also been observed in undoped samples for some compositions of the Sr(Ti,Zr)O3 solid-solution [55], so it may be related to structural changes, such as the cation-oxygen distance which depends on the relative amount Ti/Zr (see Table 2).

In the inset of Fig. 5 are displayed the spectra in the range from 400 nm to 750 nm where low-intensity absorption maxima around 450 nm, 500 nm and 600 nm ascribed to the *f-f* transitions of Pr^{3+} appear. The first maxima are ascribed to the transitions from $^3H_4$ to

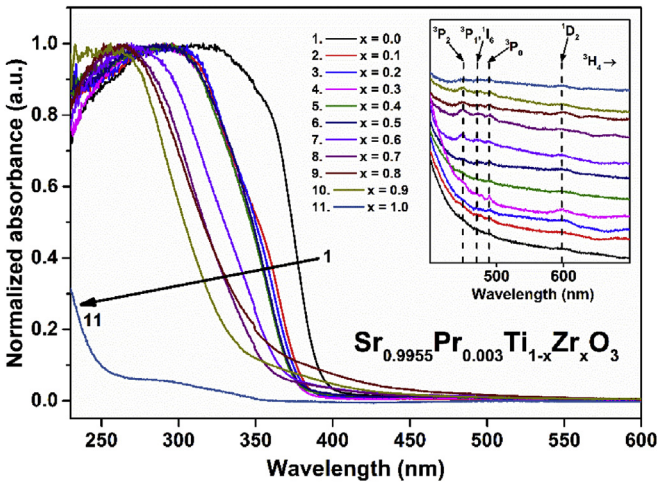

Fig. 5. UV–visible absorption spectra of SPTZO powders calcinated at 800 °C for 1 h.

$^3P_2$, ($^3P_1$, $^1I_6$), and $^3P_0$ levels of Pr^{3+}, while the maximum at ≈ 600 nm is ascribed to the transition $^3H_4 \rightarrow {}^1D_2$.

Assuming that, the sudden increase in the absorption spectra is associated with the band-to-band transition, and whose energy corresponds to the energy of the optical band gap, E_g, (hereafter referred only as the energy band gap), and except for the E_g value of $SrZrO_3$ obtained from Ref. [10], we calculate all the others E_g values of the SPTZO samples, as follows. The diffuse reflectance data were converted by the Kubelka-Munk function [56] and then the band gap energies were determined from Tauc plots [57]. In Fig. 6, the evolution of the E_g values is shown. As it is seen, there is an increase of E_g associated with the increase of the zirconium content. This behavior can be related to the differences in the binding energy of Ti-*3d* sates as compared with the Zr-*4d* states. Zr-*4d* states possess higher binding energies [55]. The valence band (VB) in STO and SZO is mainly associated with the O_{2p} states, while the conduction band (CB) is mainly due to Ti_{3d} and Zr_{4d} states. Despite the observed increase of E_g as a function of the relative Ti^{4+}/Zr^{4+} concentration, from our results of the photoluminescence spectroscopy and the approach we use to explain them (presented below), the E_g values seem to be lower than expected because the presence of a low-laying in energy state, that we ascribe to the O^{2-}-to-Ti^{4+} LMCT.

The normalized excitation spectra for all the series compounds along the solid-solution when monitoring the 489 nm ($^3P_0 \rightarrow {}^3H_4$) and the 605 nm ($^1D_2 \rightarrow {}^3H_4$) emission maxima, are presented in

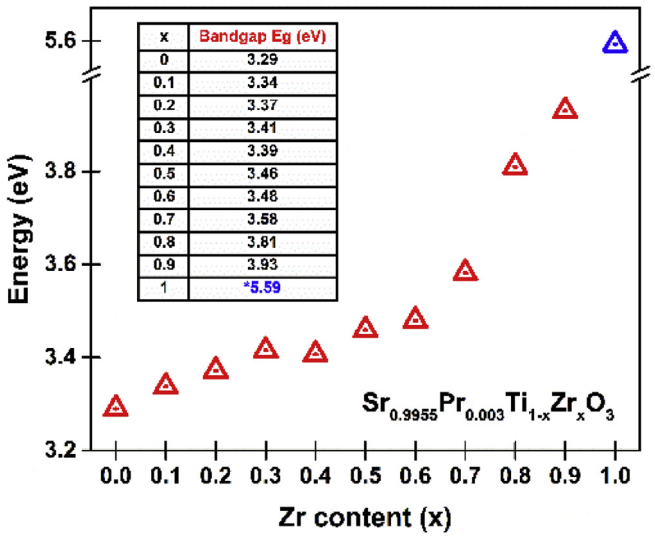

Fig. 6. Composition dependence of bandgap estimated from diffuse reflectance spectra. Notice the break in the band gap energy axis.

Fig. 7(a) and (b), respectively. Both sets of spectra show a broad band in the region of shorter wavelengths, ascribed to the interaction between Pr^{3+} and the host. Since in a previous work in Pr^{3+}-doped $SrTiO_3$ the presence of a Pr^{3+}-Ti^{4+} MMCT state is not demonstrated beyond doubt, but the presence of an O^{2-}—Ti^{4+} LMCT state it is shown [21] and after some previous results in Pr^{3+}-doped $SrZrO_3$ containing 1 mol% of Ti^{4+} [20] we ascribe that band as being due to the last charge transfer state. At this point it is important to emphasize that our ascription does not rule out the presence of the Pr^{3+}-Ti^{4+} MMCT state; however, more specific experiments as those reported in Ref. [21], and for now out of our reach, need to be performed to clarify this contentious issue.

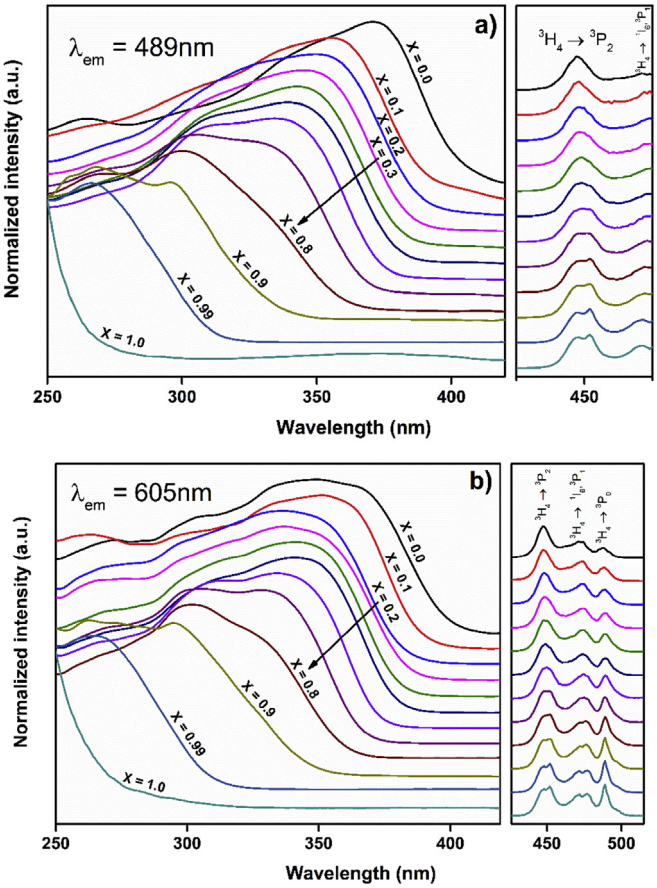

Fig. 7. Normalized excitation spectra of SPTZO powders monitoring at 489 nm ($^3P_0 \rightarrow {}^3H_4$) (a) and 605 nm ($^1D_2 \rightarrow {}^3H_4$) (b).

For the sample $Sr_{0.9955}Pr_{0.003}ZrO_3$ (x = 1.0) only the tail of the short-wavelengths-band is observed, since its maximum is supposed to appear even at shorter wavelengths, where our experimental set up is unable to go [24]. As it is seen, there is a shift of the edge of the broad band toward shorter wavelengths as the Zr^{4+} content increases. This trend is similar than that observed in the diffuse reflectance spectra, depicted in Fig. 5. On the right side of Fig. 7(a) and (b) are also observed the excitation peaks due to the *f-f* transitions of Pr^{3+}. They are assigned to the transitions from the $^3H_4$ level to the $^3P_2$, ($^3P_1$, $^1I_6$) and $^3P_0$ (only seen in Fig. 7(b)) levels.

Important to highlight, is the noticeable change between spectra corresponding to the samples with x = 1.0 and x = 0.9 (also very remarkable in Fig. 5). This change is due to addition of Ti^{4+}, and in order to illustrate its effect, in Fig. 7 are also included the spectrum of the sample $Sr_{0.9955}Pr_{0.003}Zr_{0.99}Ti_{0.01}O_3$ (x = 0.99). As we have demonstrated in a previous work [20], the addition of Ti^{4+} to SZO at low concentration, results in the formation of an O^{2-}-to-Ti^{4+} LMCT state. This state produces a band with a full width at half maximum of ~10 000 cm^{-1}, very similar in its features as those reported for many large band gap compounds where Ti^{4+} is added as a dopant [58–60]. Since the energy of the O^{2-}-to-Ti^{4+} LMCT state is lower than the energy associated with the O^{2-}-to-Zr^{4+} LMCT state, in our opinion this is the reason why there is an important shift in the edge of the excitation and absorption bands, associated with the host, between samples with x = 0.9 and SZO (x = 1.0). In the same way, we are convinced this could be the reason for the lower values of E_g (Fig. 6) obtained for compositions containing Ti^{4+}. Apart from the SPTO sample, where the energy of the O^{2-}-to-Ti^{4+} LMCT state must correspond to the energy required to excite electrons from the valence band to the exciton level [14], in all the other compositions containing Ti^{4+}, the O^{2-}-to-Ti^{4+} LMCT state would be defining the edge of the absorption and excitation bands associated with the host, but they not necessarily should

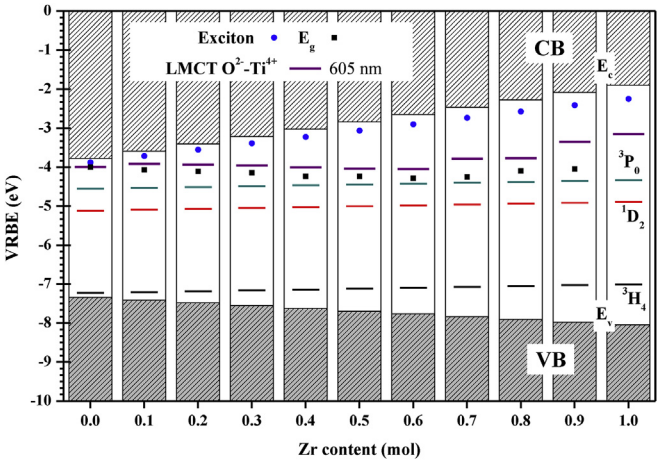

Fig. 8. Stacked VRBE diagrams for the series compounds of the $Sr_{0.9955}Pr_{0.003}Ti_{1-x}Zr_xO_3$ solid-solution. Ev, Ec and E_{ex} represent the binding energies of the top of the valence band (VB), the bottom of the conduction band (CB), and the exciton state, respectively. The binding energies for the representative levels of the Pr^{3+}, $^3H_4$, $^1D_2$, and $^3P_0$, the Eg values (inset of Fig. 6), and the energy of the O^{2-}-to-Ti^{4+} LMCT state derived from the excitation spectra measured at λ_{em} = 605 nm are also plotted. The energy of the O^{2-}-to-Ti^{4+} LMCT for sample with x = 1, corresponds to sample with x = 0.99.

correspond with the transition from the valence band to the exciton level, which is exactly as E_g is defined. In any case, the edge of the interband transition would be masked by the strong band related to the O^{2-}-to-Ti^{4+} LMCT state as it has already been reported [20].

To present a semi quantitative explanation of the previous results, also useful for discussing the results to be presented, we construct the scheme of Fig. 8 following the approach of the chemical shift model formulated by Dorenbos [35,37,61]. In general terms, the chemical shift model allows the location, referred to a unique energy reference, the vacuum binding energy, of: 1) the top of the valence and bottom of conduction bands, and the exciton level of the host, 2) the 4f-energy-levels of divalent and trivalent lanthanides, and 3) the energy levels due to many other doping ions. In Fig. 8 are shown the stacked vacuum referred electron binding energies (VRBE) diagrams of the solid-solution SPTZO series compounds.

The diagrams of Fig. 8 are plotted from ours and those experimental data adapted from previous reports [10,54]. All these data are summarized in Table 3. To fix the VRBE values of the top of the valence band, the bottom of the conduction band, the exciton level and the energy levels of Pr^{3+}, we perform a linear interpolation, as a function of x, i.e. the content of Zr^{4+} in the solid-solution, between the data previously reported for STO [54] and SZO [10]. In Fig. 8, referred to the binding energy at the top of the valence band, is plotted the value of the energies obtained from the maxima at the highest wavelength of the excitation spectra for each compound when $\lambda_{em} = 605$ nm. It is important to notice the similarity among these values and those obtained from excitation spectra when $\lambda_{em} = 489$ nm (see Table 3), they are the same if measurement errors are taken into account, which are supposed to be around a few tenths of eV [62]. It is also clear the mismatch between the energy of the exciton state, E_{ex}, and the energy obtained from the excitation spectra. Even more noticeable, it is the difference between the values of the energies E_g and E_{ex}, which ideally should be the same. We think that the main cause of both disagreement is associated with the low-lying in energy LMCT (O^{2-}-to-Ti^{4+}) state due to the presence of Ti^{4+}, that as above-mentioned, mask the actual band associated with the interband transition. Thus, we assign the energy values obtained from the excitation spectra to the O^{2-}-to-Ti^{4+} LMCT state. Supporting the plausibility of the VRBE diagram of Fig. 8, and considering that typical errors in this type of diagrams are around few tenths of eV [62], there are the next two important facts. The energies of the exciton level, E_{ex}, the band gap E_g, and the O^{2-}-to-Ti^{4+} LMCT state, have similar values for SPTO; and the energy values associated with the O^{2-}-to-Ti^{4+} LMCT transition for samples with x from 0.1 to 0.8, are around − 4 eV as it is expected [14]. The energy value of the O^{2-}-to-Ti^{4+} LMCT state for the sample with $x = 0.9$ is −3.25 eV, which is greater than those of samples containing more Ti^{4+}, but similar to the value of −3.15 eV found for the sample with $x = 0.99$ (showed in the VRBE diagram of the sample with $x = 1.0$).

The first effect on the luminescent response of the SPTZO solid-solution as the Zr^{4+} increases, is seen in the excitation spectra (not normalized) for the representative transitions $^3P_0 \rightarrow {}^3H_4$ ($\lambda_{em} = 489$ nm) and $^1D_2 \rightarrow {}^3H_4$ ($\lambda_{em} = 605$ nm) depicted in Fig. 9. In these spectra, a continuous increase in the luminescence intensity from $x = 0.0$ to $x = 0.5$, and then a decrease from $x = 0.5$ to $x = 0.9$ are observed. Since such behavior occurs for both transitions, it is attributed to changes in the interaction between the f-f transitions of Pr^{3+} and the host. Those changes are mainly due to the modifications in the electronic structure of the host, associated, in turn, with the change in the crystal structure induced by the incorporation of Zr^{4+}. Those structural-related modifications, lead to favor the energy transfer from the host to the Pr^{3+}, and reaches a maximum for the sample with $x = 0.5$. In this regard, Fig. 8 seems to give some clue about the excitation behavior. As the energy

Table 3
Optical properties of the SPTZO series compounds. These data serve as input for the construction of the stacked VRBE diagrams showed in Fig. 8. The values given in eV are all relatives to the vacuum.

x (mol)	E_v (eV)[a]	E_c (eV)[a]	E_{ex} (eV)[a]	$^3H_4$ (eV)[a]	E_g (eV)[b]	LMCT ($\lambda_{em} = 605$ nm) (nm)[c] (eV)[d]	LMCT ($\lambda_{em} = 489$ nm) (nm)[e] (eV)[f]
0.0	−7.34	−3.78	−3.88	−7.23	−4.05	371.0 −4.00	350.0 −3.80
0.1	−7.41	−3.5	−3.72	−7.21	−4.07	355.0 −3.92	350.0 −3.87
0.2	−7.48	−3.40	−3.55	−7.19	−4.11	350.0 −3.94	338.0 −3.81
0.3	−7.55	−3.22	−3.39	−7.16	−4.14	345.0 −3.96	336.0 −3.86
0.4	−7.62	−3.03	−3.23	−7.14	−4.23	343.0 −4.01	337.0 −3.94
0.5	−7.69	−2.84	−3.06	−7.12	−4.23	339.0 −4.04	338.0 −4.03
0.6	−7.77	−2.65	−2.90	−7.10	−4.29	334.0 −4.05	334.0 −4.05
0.7	−7.84	−2.46	−2.74	−7.08	−4.26	306.0 −3.78	304.0 −3.76
0.8	−7.91	−2.28	−2.58	−7.05	−4.10	300.0 −3.77	302.0 −3.80
0.9	−7.98	−2.09	−2.41	−7.03	−4.05	268.0 −3.35	264.0 −3.29
1.0	−8.05	−1.90	−2.25	−7.01	−2.46	253.0 −3.15	253.0 −3.15

[a] Values correspond to linear interpolation between data reported in Ref. [54] for $SrTiO_3$ ($x = 0$) and data reported in Ref. [10] for $SrZrO_3$ ($x = 1$).
[b] Values result from the addition of Ev and the data of the inset in Fig. 6.
[c] Data obtained from the maxima of the excitation spectra of Fig. 7(b).
[d] Values in eV result of adding Ev and the equivalent in eV of the corresponding wavelength of the maxima in the excitation spectra.
[e] Similar to c, but for excitation spectra of Fig. 7(a).
[f] Values in eV calculated in the same way as explained in d.

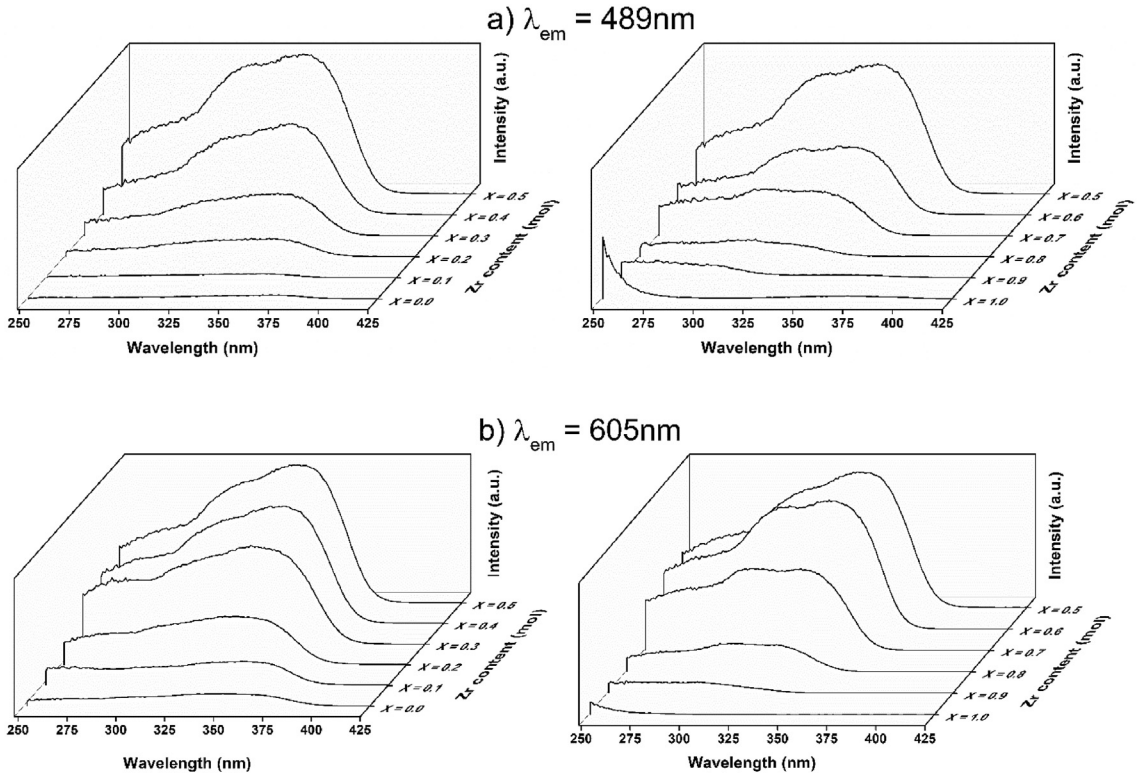

Fig. 9. Excitation spectra corresponding to the host of SPTZO, when monitored at 489 nm ($^3P_0 \rightarrow {}^3H_4$) (a), and at 605 nm ($^1D_2 \rightarrow {}^3H_4$) (b). Important to notice is that the values of x (front to back) increase in the spectra on the left from 0.0 to 0.5 and decrease in the spectra on the right from 1.0 to 0.5.

difference between the O^{2-}-to-Ti^{4+} LMCT state and the levels of Pr^{3+} decreases from x = 0.0 to x = 0.5, the energy transfer from the host to Pr^{3+} is more efficient and the excitation intensity increases. However, from x = 0.6 to x = 0.9 that difference in energy again increases making the transfer of energy more difficult; thus, the excitation intensity once more decreases.

The second effect, also reveled in the excitation spectra, but associated with the *f-f* transition of Pr^{3+} is shown in Fig. 10. As it is observed, the participation in the activation of the $^3P_0 \rightarrow {}^3H_4$ ($\lambda_{em} = 489$ nm) transition via the *f-f* energy levels increases (except for the sample with x = 0) as the content of Zr^{4+} increases in the solid solution. On the opposite way, the contribution of those levels to the activation of the $^1D_2 \rightarrow {}^3H_4$ ($\lambda_{em} = 605$ nm) transition decreases as the content of Zr^{4+} increases. We attribute this complementary behavior to the relative Ti/Zr concentration.

Regarding the emission of Pr^{3+}, we found very interesting results. When samples containing Ti^{4+} (x = 0 to x = 0.9) were excited through the host band, always the dominant emission is that ascribed to the red $^1D_2 \rightarrow {}^3H_4$ transition as it is shown in Fig. 11. This result can be explained in simple terms. As previously described, the host-excitation band for samples containing Ti^{4+} is governed by the low-laying in energy LMCT (O^{2-}-to-Ti^{4+}) state. Recently, and refuting the accepted idea of the origin of the dominant red emission in Pr^{3+}-doped titanates, evidence has been presented indicating that at least one component of the LMCT (O^{2-}-to-Ti^{4+}) state laying between the $^3P_0$ and $^1D_2$ levels of Pr^{3+} can be

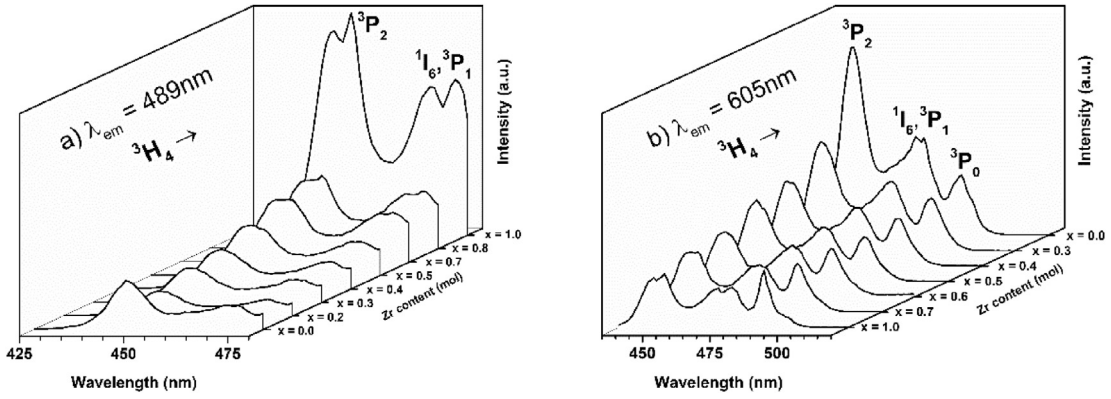

Fig. 10. Excitation spectra corresponding to the f-f transitions of Pr^{3+} SPTZO, when monitored at 489 nm ($^3P_0 \rightarrow {}^3H_4$) (a), and at 605 nm ($^1D_2 \rightarrow {}^3H_4$) (b). Important to notice is that the values of x (front to back) increase in the spectra on the left from 0.0 (SPTO) to 1.0 (SPZO) and decrease in the spectra on the right from 1.0 to 0.0.

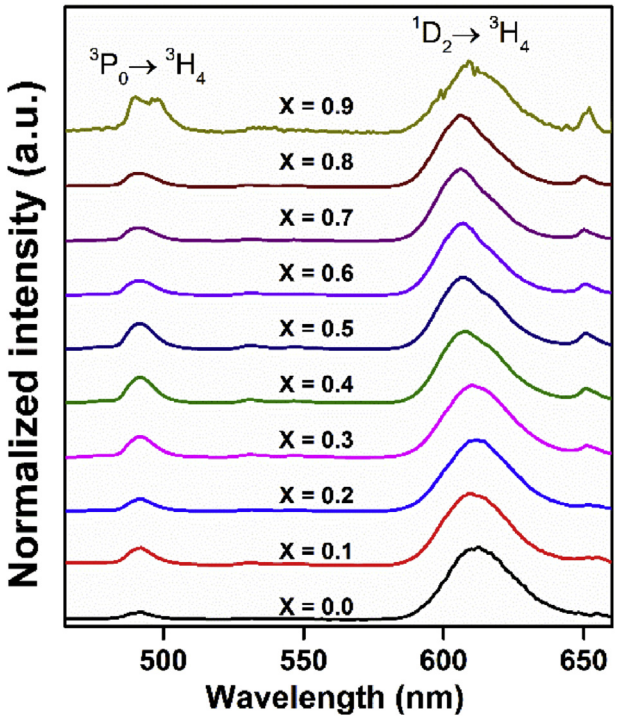

Fig. 11. Emission spectra of samples SPTZO ($x = 0$ to $x = 0.9$, i.e. only of those containing Ti^{4+}). For sample $x = 0.9$, $\lambda_{exc} = 260$ nm. For all the other samples $\lambda_{exc} = 340$ nm.

responsible for the dominance of the $^1D_2 \rightarrow {}^3H_4$ transition in the luminescent response of $CaTiO_3$:Pr^{3+} by providing an efficient nonradiative decay mechanism to selectively populate the $^1D_2$ state [19]. Thus, we attribute the red dominance in the emission spectra of Fig. 11 to the same argument; although the Pr^{3+}-Ti^{4+} MMCT could not be completely ruled out to be playing a role in this process. However, no obvious evidence of the Pr^{3+}-Ti^{4+} MMCT as that one found for the O^{2-}-to-Ti^{4+} LMCT is present in the absorption and emission spectra we measure.

In Fig. 12, the normalized emission spectra for the SPTZO samples when excited through the $^3H_4 \rightarrow {}^3P_2$ transition of Pr^{3+} at 447 nm are shown. In this case, the emission exhibits a modulation between the $^1D_2 \rightarrow {}^3H_4$ and $^3P_0 \rightarrow {}^3H_4$ bands as x increases. For

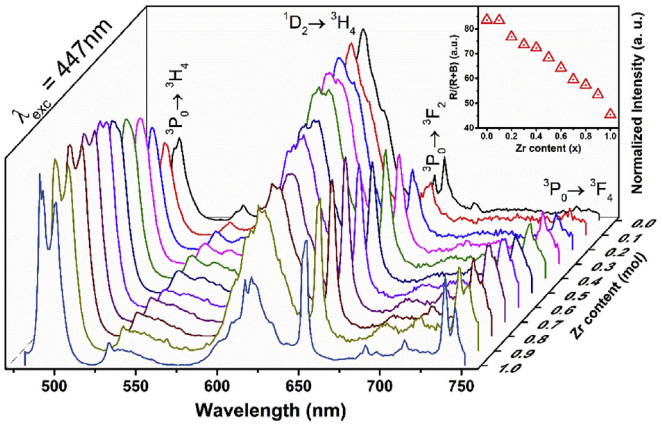

Fig. 12. Emission spectra (λ_{exc} = 447 nm) of SPTZO. Inset shows R/(R+B) ratio as a function of x. R and B are the integrated areas of the red and green-bluish bands in the spectra. (For interpretation of the references to color in this figure legend, the reader is referred to the Web version of this article.)

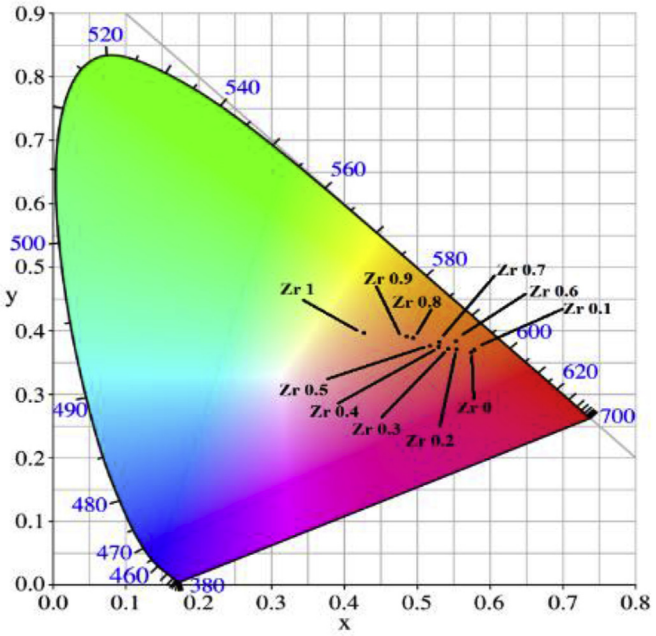

Fig. 13. Color space CIE 1931, where the color coordinates corresponding to all the compositions of the SPTZO solid solution are indicated. (For interpretation of the references to color in this figure legend, the reader is referred to the Web version of this article.)

$x = 0$ the emission is practically dominated by the $^1D_2 \rightarrow {}^3H_4$ as it is expected in Pr^{3+}-doped titanates. However, as the Zr^{4+} increases, the band ascribed to the $^3P_0 \rightarrow {}^3H_4$ transition gradually gains intensity in comparison to the band due to the $^1D_2 \rightarrow {}^3H_4$ transition, and finally becomes dominant for the sample with $x = 1.0$. Since another bands ascribed to the transitions $^3P_0 \rightarrow {}^3H_6$ and $^3P_1 \rightarrow {}^3F_2$ overlap with the $^1D_2 \rightarrow {}^3H_4$ peak, its position is indicated by the arrow in Fig. 12. As it is seen, the intensity at this point is very weak for the SPZO ($x = 1.0$) sample. These results observed for the end compositions of the SPTZO solid-solution agree with those previously reported for $SrTiO_3$ [21] and $SrZrO_3$ [20,24] doped with Pr^{3+}.

In order to know the relative contribution of the $^3P_0 \rightarrow {}^3H_4$ and $^1D_2 \rightarrow {}^3H_4$ bands, denoted as B (greenish-blue) and R (red), in the inset of Fig. 12 the intensity ratio R/R(R+B) is plotted as function of x. R and B were calculated by integrating the areas of the red and greenish-blue emission bands, respectively. As expected, the magnitude of the R/R(R+B) ratios decreases as x increases.

Finally, taking advantage of the modulation in the intensity of the emission associated with the transitions $^3P_0 \rightarrow {}^3H_4$ and $^1D_2 \rightarrow {}^3H_4$ we assess the color features of the SPTZO solid-solution series compounds. Fig. 13 shows the color coordinates, CIE 1931, for the entire series plotted in its corresponding color space. In the figure, it is clearly seen the impact of the stoichiometry in the tuning of the luminescent properties.

4. Conclusions

Polycrystalline powder samples of $Sr_{0.9955}Pr_{0.003}Ti_{1-x}Zr_xO_3$ ($0.0 \leq x \leq 1.0$) solid-solution were synthesized by the Pechini method at 800 °C for 1 h. The Rietveld analyses allow to establish the crystal structure for the entire solid-solution SPTZO. Three crystal phases were found, cubic (*Pm-3m*) from $x = 0.0$ to $x = 0.2$, tetragonal (*I4/mcm*) from $x = 0.3$ to $x = 0.5$, and orthorhombic (*Pnma*) from $x = 0.6$ to $x = 1.0$. The estimated average crystal size was smaller than 100 nm for all compositions. The optical

properties of the compounds are reasonable explained using the chemical shift model. This model allows us to explain that the smaller the difference in energy between the O^{2-}-to-Ti^{4+} LMCT state and the higher levels of Pr^{3+} is, the more efficient the energy transfer from the host to Pr^{3+} is. The dominance of the $^1D_2 \rightarrow {}^3H_4$ transition in samples containing Ti^{4+} when excited through the host, are related with the low-laying in energy O^{2-}-to-Ti^{4+} LMCT state. Although we do not discard the existence of the Pr^{3+}-Ti^{4+} MMCT, we do not find obvious evidence of its presence in the absorption and excitation spectra. In order to establish or rule out its presence, additional experiments need to be performed. On the other hand, a modulation between the emission associated with the $^3P_0 \rightarrow {}^3H_4$ and $^1D_2 \rightarrow {}^3H_4$ transitions as a function of x when samples are excited via the $^3H_4 \rightarrow {}^3P_2$ transition at 447 nm, is demonstrated. As we finally showed, this behavior allows the tuning of the color of the emission as a function of the chemical composition of the SPTZO series compounds.

Acknowledgements

Germán López-Pacheco and Federico González are grateful to CONACyT-México for granting them scholarships for the PhD (CVU 485626) and for a sabbatical stay (CVU 89843-472353), respectively. The authors thank CONACyT-México for providing financial support under CB-154962, CB-2011-1 No. 166108 and INFR 163250 projects and PAPIIT-UNAM (IN102715). Also, special thanks to Omar Novelo (IIM-UNAM) for SEM image acquisition, and the XRD Laboratory (T-128) UAM-I for the XRD measurements.

References

[1] A. Durán, E. Martínez, J.A. Díaz, J.M. Siqueiros, Ferroelectricity at room temperature in Pr-doped $SrTiO_3$, J. Appl. Phys. 97 (2005), 104109.
[2] C. Wang, H. Qiu, T. Inoue, Q. Yao, Band gap engineering of $SrTiO_3$ for water splitting under visible light irradiation, Int. J. Hydrogen Energy 39 (2014) 12507–12514.
[3] A. Sendil Kumar, P. Suresh, M. Mahesh Kumar, H. Srikanth, M.L. Post, K. Sahner, R. Moos, S. Srinath, Magnetic and ferroelectric properties of Fe doped $SrTiO_{3-\delta}$ films, J. Phys. Conf. 200 (2010), 092010.
[4] Y. Yamada, Y. Kanemitsu, Band-to-band photoluminescence in $SrTiO_3$, Phys. Rev. B 82 (2001), 121103(R).
[5] A. West, Solid State Chemistry and its Applications, 2nd. Edition, 2014.
[6] M. Johnsson, P. Lemmens, Crystallography and Chemistry of Perovskites, Handbook of Magnetism and Advanced Magnetic Materials, 2006, pp. 2098–2106.
[7] P. Schlotter, R. Schmidt, J. Schneider, Luminescence conversion of blue light emitting diodes, Appl. Phys. A 64 (1997) 417–418.
[8] Q.Y. Zhang, X.Y. Huang, Recent progress in quantum cutting phosphors, Prog. Mater. Sci. 55 (2010) 353–427.
[9] C. Humphreys, Solid-state lighting, MRS Bull. 33 (2008) 459–470.
[10] P. Dorenbos, The electronic structure of lanthanide doped compounds with 3d, 4d, 5d, or 6d conduction band states, J. Lumin. 151 (2014) 224–228.
[11] P.S. Peijzel, A. Meijerink, R.T. Wegh, M.F. Reid, G.W. Burdick, A complete $4f^n$ energy level diagram for all trivalent lanthanide ions, J. Solid State Chem. (2005) 448–453.
[12] A. Ellens, H. Andres, A. Meijerink, G. Blasse, Spectral-line-broadening study of the trivalent lanthanide-ion series. I. Line broadening as a probe of the electron-phonon coupling strength, Phys. Rev. B 55 (1997) 173.
[13] P. Dorenbos, Energy of the first $4f^7 \rightarrow 4f^6$ 5d transition of Eu^{2+} in inorganic compounds, J. Lumin. 104 (2003) 239–260.
[14] E.G. Rogers, P. Dorenbos, Vacuum energy referred $Ti^{3+/4+}$ donor/acceptor states in insulating and semiconducting inorganic compounds, J. Lumin. 153 (2014) 40–45.
[15] E. Pinel, P. Boutinaud, R. Mahiou, What makes the luminescence of Pr^{3+} different in $CaTiO_3$ and $CaZrO_3$? J. Alloys. Compd. 380 (2004) 225–229.
[16] E.G. Reut, A.I. Ryskin, Virtual recharge: mechanism of radiationless transition in scheelite and fergusonite type crystals doped with rare-earth ions, Phys. Stat. Sol. A 17 (1973) 47.
[17] R. Boutinaud, E. Mahiou, M. Cavalli, Bettinelli, Luminescent properties of Pr^{3+} in titanates and vanadates: towards a criterion to predict $^3P_0$ emission quenching, Chem. Phys. Lett. 418 (2006) 185–188.
[18] P. Boutinaud, L. Sarakha, E. Cavalli, M. Betinelli, P. Dorenbos, R. Mahiou, About red afterglow in Pr3+ doped titanate perovskites, J. Phys. D Appl. Phys. 42 (2009), 045106.
[19] Z. Barandiarán, M. Bettinelli, L. Seijo, Color control of Pr^{3+} luminescence by electron–hole recombination energy transfer in $CaTiO_3$ and $CaZrO_3$, J. Phys. Chem. Lett. 8 (2017) 3095–3100.
[20] T.J. Pérez-Juache, R. López-Juárez, E. Barrera-Calva, F. González, Luminescent properties of Pr^{3+}-doped $SrZrO_3$ phosphors, J. Lumin. 192 (2017) 599–607.
[21] Y. Katayama, J. Ueda, S. Tanabe, Photo-electronic properties and persistent luminescence in Pr^{3+} doped (Ca,Sr)TiO_3 ceramics, J. Lumin. 148 (2014) 290–295.
[22] T. Kyômen, R. Sakamoto, N. Sakamoto, S. Kunugi, M. Itoh, Photoluminescence properties of Pr-Doped (Ca,Sr,Ba)TiO_3, Chem. Mater. 17 (2005) 3200–3204.
[23] L. Lin, B. Yan, Sol–gel synthesis and photoluminescence of $CaTi_{1-x}Zr_xO_3$: Pr^{3+} phosphors, Bull. Mater. Sci. 33 (2010) 79–83.
[24] Y. Jin, Y. Hu, L. Chen, X. Wang, G. Ju, Z. Mou, Luminescence properties of dual-emission (uv/visible) long afterglow phosphor SrZrO3:Pr^{3+}, J. Am. Ceram. Soc. 96 (2013) 3821–3827.
[25] H. Guo, N. Dong, M. Yin, W. Zhang, L. Lou, S. Xia, Photoluminescence Green and red upconversion luminescence in Er3+-doped and Er3+/Yb3+-codoped SrTiO 3 ultrafine powders, J. Alloys Compd. 415 (2006) 280–283.
[26] S.K. Gupta, A.K. Yadav, D. Bhattacharya, S.N. Jha, V. Natarajan, Visible light emitting Ln3+ ion (Ln=Sm, Eu and Dy) as a structural probe: a case study with SrZrO3, J. Lumin. 164 (2015) 1–22.
[27] L. Rimai, G.A. deMars, Electron paramagnetic resonance of trivalent gadolinium ions in strontium and barium titanates, Phys. Rev. 127 (1962) 702.
[28] C. Howard, K. Knight, B. Kennedy, E. Kisi, The structural phase transitions in strontium zirconate revisited, J. Phys. Condens. Matter 12 (2000) L677–L683.
[29] T.K.-Y. Wong, B. Kennedy, C. Howard, B. Hunter, T. Vogt, Crystal structures and phase transitions in the $SrTiO_3$–$SrZrO_3$ solid solution, J. Solid State Chem. 156 (2001) 255–263.
[30] R. Mc Knight, B. Kennedy, Q. Zhou, M. Carpenter, Elastic anomalies associated with transformation sequences in perovskites: II. The strontium zirconate–titanate Sr(Zr,Ti)O_3 solid solution series, J. Phys. Condens. Matter 21 (2009), 015902.
[31] Z. Zhang, J. Koppensteiner, W. Schranz, M.A. Carpenter, Anelastic loss behaviour of mobile microstructures in $SrZr_{1-x}Ti_xO_3$ perovskites, J. Phys. Condens. Matter 22 (2010), 295401.
[32] C.W. Thiel, H. Cruguel, H. Wu, Y. Sun, G.J. Lapeyre, R.L. Cone, R.W. Equall, R.M. MacFarlane, Phys. Rev. B Condens. Matter. 64 (2001), 085107.
[33] C.W. Thiel, H. Cruguel, Y. Sun, G.J. Lapeyre, R.M. MacFarlane, R.W. Equall, R.L. Cone, J. Lumin. 94 (2001) 1–6.
[34] C.W. Thiel, R.L. Cone, J. Lumin. 131 (2011) 386–395.
[35] P. Dorenbos, Modeling the chemical shift of lanthanide 4f electron binding energies, Phys. Rev. B 85 (2012), 165107.
[36] P. Dorenbos, A. Krumpel, E. van der Kolk, P. Boutinaud, M. Bettinelli, E. Cavalli, Lanthanide level location in transition metal complex compounds, Opt. Mater. 32 (2010) 1681–1685.
[37] P. Dorenbos, A review on how lanthanide impurity levels change with chemistry and structure of inorganic compounds, ECS J. Solid State Sci. Technol. 2 (2013) R3001–R3011.
[38] P. Dorenbos, E. Rogers, Vacuum referred binding energies of the lanthanides in transition metal oxide compounds, ECS J. Solid State Sci. Technol. 3 (2014) R150–R158.
[39] N. George, K. Denault, R. Seshadri, Phosphors for solid-state white lighting, Annu. Rev. Mater. Res. 43 (2013) 481–501.
[40] M.H. Crawford, LEDs for solid-state lighting: performance challenges and recent advances, IEEE J. Sel. Top. Quant. Electron. 5 (2009) 1028.
[41] M. Krames, O. Shchekin, R. Mueller-Mach, G. Mueller, L. Zhou, G. Harbers, M.G. Craford, Status and future of high-power light-emitting diodes for solid-state lighting, J. Disp. Technol. 3 (2007) 160–175.
[42] X. Chen, Z. Xia, Synthesis and color-tunable luminescence of Ce^{3+}, Tb^{3+} codoped $Sr_6YSc(BO_3)_6$ phosphor, J. Solid State Light. 1 (2014) 4.
[43] M. Pechini, Method of preparing lead and alkaline earth titanates and niobates and coating method using the same to form a capacitor, Patent US 3330697 A, (1963).
[44] W. Dabrowski, P. Grybos, P. Hottowy, K. Swientek, P. Wiacek, Integrated readout of silicon strip detectors for position sensitive measurement of X-rays, Nucl. Instrum. Methods Phys. Res. Sect. A 512 (2003) 213–219.
[45] R. Cheary, A. Coelho, A fundamental parameters approach to X-ray line-profile fitting, J. Appl. Crystallogr. 25 (1992) 109–121.
[46] TOPAS V4.2: General Profile and Structure Analysis Software for Powder Diffraction Data, User's manual, Bruker AXS, Karlsruhe, Germany, 2009.
[47] D. Black, D. Windover, A. Henins, J. Filliben, J. Cline, Certification of standard reference material 660B, Nat. Inst. Stand. Technol. 26 (2011) 155–158.
[48] G. Hölzer, M. Fritsch, M. Deutsch, J. Härtwig, E. Förster, $K\alpha_{1,2}$ and $K\beta_{1,3}$ x-ray emission lines of the 3d transition metals, Phys. Rev. 56 (1997) 4554.
[49] M. Järvinen, Application of symmetrized harmonics expansion to correction of the preferred orientation effect, J. Appl. Crystallogr. 26 (1993), 525–231.
[50] Prince, Comparison of profile and integrated-intensity methods in powder refinement, J. Appl. Crystallogr. 14 (1981) 157–159.
[51] R. Shannon, Revised effective ionic radii and systematic studies of interatomic distances in halides and chalcogenides, Acta. Cryst. A A 32 (1976) 751–767.
[52] R. Mitchell, A. Chakhmouradian, A new Series of complex perovskites $La_{1-x}Sr_xCr_{1-x}Ti_xO_3$: structural characterization, J. Solid State Chem. 144 (1999) 81–85.
[53] R.A. Young, The Rietveld Method, International Union Crystallography, Oxford Science Publications, 1995.
[54] P. Dorenbos, The electronic structure of lanthanide impurities in TiO_2, ZnO,

SnO_2, and related compounds, ECS J. Solid State Sci. Technol. 3 (2014) R19–R24.
[55] Y. Yang, S. Luo, F. Dong, Y. Ding, X. Li, Synthesis of high-phase purity $SrTi_{1-x}Zr_xO_3$ ceramics by sol-spray pyrolysis method, Mater. Manuf. Process. 30 (2015) 585–590.
[56] P. Kubelka, F. Munk, Ein Beitrag zur Optik der Farbanstriche, Z. Tech. Phys. 12 (1931) 593–601.
[57] J. Tauc, R. Grigorovic, A. Vancu, Optical properties and electronic structure of amorphous germanium, Phys. Stat. Sol. 15 (1966) 627–637.
[58] A. Macke, Investigations on the luminescence of titanium-activated stannates and zirconates, J. Solid State Chem. 18 (1976) 337–346.
[59] L. de Haart, A. de Vries, G. Blasse, On the photoluminescence of semiconducting titanates applied in photoelectrochemical cells, J. Solid State Chem. 59 (1985) 291–300.
[60] Y. Cong, B. Li, X. Wang, B. Lei, W. Li, Synthesis and optical property studies of nanocrystalline ZrO_2:Ti long-lasting phosphors, J. Electrochem. Soc. 155 (2008) K195–K198.
[61] E.G. Rogers, P. Dorenbos, Vacuum referred binding energy of the single 3d, 4d, or 5d electron in transition metal and lanthanide impurities in compounds, ECS J. Solid State Sci. Technol. 3 (2014) R173–R184.
[62] J.J. Joos, D. Poelman, P.F. Smet, Energy level modeling of lanthanide materials: review and uncertainty analysis Phys, Chem. Chem. Phys. 17 (2015) 19058.